Research Article | Vol. 26, No. 22 | 29 Oct 2018 | OPTICS EXPRESS 29363
Optics EXPRESS

# Implementation of plasmonic band structure to understand polariton hybridization within metamaterials

NICHOLAS SHARAC,[1] ALEXANDER J. GILES,[2] KEITH PERKINS,[2] JOSEPH TISCHLER,[2] FRANCISCO BEZARES,[1,3] SHARKA M. PROKES,[2] THOMAS G. FOLLAND,[4] OREST J. GLEMBOCKI,[2] AND JOSHUA D. CALDWELL[2,4]

[1]*ASEE/NRC Postdoctoral fellow, residing at NRL, Washington, DC, USA*
[2]*U.S. Naval Research Laboratory, Washington, DC 20375, USA*
[3]*University of Puerto Rico, Cayey, PR, 00736, USA*
[4]*Dept. of Mechanical Engineering, Vanderbilt University, Nashville, TN 37212, USA*
[*]*josh.caldwell@vanderbilt.edu*

**Abstract:** Gap surface plasmons (GSPs) serve a diverse range of plasmonic applications, including energy harvesting, communications, molecular sensing, and optical detection. GSPs may be realized where tightly spaced plasmonic structures exhibit strong spatial overlap between the evanescent fields. We demonstrate that within similar, nested geometries that the near-fields of the GSPs within the individual nanostructures are hybridized. This creates two or more distinct resonances exhibiting near-field distributions extended over adjacent spatial regions. In contrast, dissimilar, nested structures exhibit two distinct resonances with nominally uncoupled near-fields, resulting in two or more individual antenna resonance modes. We deploy plasmonic band structure calculations to provide insight into the type and degree of hybridization within these systems, comparing the individual components. This understanding can be used in the optimized design of polaritonic metamaterial structures for desired applications.

© 2018 Optical Society of America under the terms of the OSA Open Access Publishing Agreement

## 1. Introduction

Surface plasmon polaritons (SPPs) exist as a quasi-particle resulting from the coupling of collective electron/hole oscillations and incident photons, which at visible and near-IR wavelengths can be stimulated and induced to propagate along a metal/dielectric interface [1–3]. Through the formation of the SPP, the wavelength of the light can be compressed to values much shorter than that of free-space light, resulting in a strong focusing of the optical electromagnetic fields. Gap surface plasmons (GSPs) are propagating SPPs that exist within a dielectric gap between two metals [4–12]. Much like a metal-insulator-metal waveguide, the overlap between the evanescent fields of the two plasmonic metal edges or nanostructures within the central dielectric gap allows for a further focusing and enhancement of the corresponding plasmonic 'hot-spot'. However, unlike neighboring nanostructures, GSPs can be established over extended lengths between a variety of plasmonic structures, such as waveguides, grooves, nanowire and nanoantenna arrays, and thus can provide large spatial areas with high local enhancements of the electromagnetic fields. These GSPs can play an important role in a diverse number of applications such as so-called 'perfect-absorbers' [13,14], enhanced spectroscopy, (e.g. surface enhanced Raman spectroscopy (SERS) [15–19] and surface enhanced infrared absorption (SEIRA) [20–23]), and monochromatic cloaking designs [24].

Coupling effects between different geometric GSPs have been explored in the case of nanogaps or slits placed within a metal-insulator-metal (MIM) configuration [8,10,25–27], and in nanogap arrays [25,28–30]. However, the influence of coupling between GSP modes of varying geometries, particularly at the level of the unit cell within a periodic metamaterial, have to this point been unexplored. Here, we study such coupling between GSPs formed in

#335873 https://doi.org/10.1364/OE.26.029363
Journal © 2018 Received 27 Jun 2018; revised 6 Aug 2018; accepted 14 Aug 2018; published 26 Oct 2018

Optics EXPRESS

nested structures of similar and dissimilar geometries within a two-dimensional metal-insulator-metal grating. Significantly, the plasmonic band structure provides an invaluable tool in evaluating the effect of the unit cell in such nested structures [31–33]. In essence, this allows one to calculate the simplified dispersion relationship for all the optical modes, thereby providing significant insight into the origin and character of each. This includes the confinement, relative group velocity (localized vs. propagating), and Poynting vector (direction of power flow), and how well a mode will survive reduced periodicity, based on its group velocity. This analysis provides simultaneous spectral and field profile qualifications, which can be used for specific applications, for example with upconversion processes. Alternatively, one could tailor similar geometries with hybridized GSP resonances to enhance the fundamental absorption and the desired emission processes in the same location simultaneously. Additionally, mode character determination, in terms of localized vs. propagating properties, can be directly quantified in terms of group velocity (slope) from the band structure calculations, while similar quantitative insights are much more complicated when extracting this data from simulated field profiles and spectra.

Here, all GSP effects are measured in grating-insulator metamaterial (GIM) geometries [34,35], featuring three different 2D square grating arrays. As originally demonstrated by both Hao et al. and Liu et al. [36,37], the GIM structure consists of the top patterned metamaterial grating design, with an underlying dielectric and bottom metallic back-reflector. We modify the grating at the level of the unit cell, by adding a secondary opening (the nested geometry) that is either dissimilar or similar to the opening of the original grating, allowing us to compare two fundamentally different unit cell modifications. Therefore, the grating unit cell consists of either a simple square (‘box’), that serves as the control, a nested, open cross within a square grating element (‘cross-in-box’ or ‘cross’; dissimilar geometries), and a square within an outer square frame (‘box-in-box’ or ‘BIB’; similar geometries). SEM images of representative structures are provided in Fig. 1(a)-1(c). Using far-field reflectance spectroscopy accompanied with electromagnetic simulations, including calculated band structures, we demonstrate that a strong hybridization of the GSPs is realized within unit cells with complementary nested geometries, e.g. the BIB structure, providing a coupling between spatially distinct regions at different resonant frequencies [38–40]. Such hybridization is absent from the simple box and nested structure with dissimilar geometries (cross structure), the latter which provides, independent resonances with distinct, resonant responses. Exploring these nested geometries enables a more comprehensive understanding of the interactions in GSP dynamics at the unit cell level and how one can use spatial and spectral hybridization of polaritonic modes to design metamaterial structures using band structure analysis. The high confinement of the modes in the dielectric layer of the GIM structure supports polaritonic modes exhibiting both localized and traveling behavior, with the resonances dispersed across the visible and near-IR. This work offers significant advances in the design of nested plasmonic grating structures that offer promise for advanced applications such as multifrequency molecular sensing, energy harvesting, and enhanced thin film IR detectors.

Optics EXPRESS

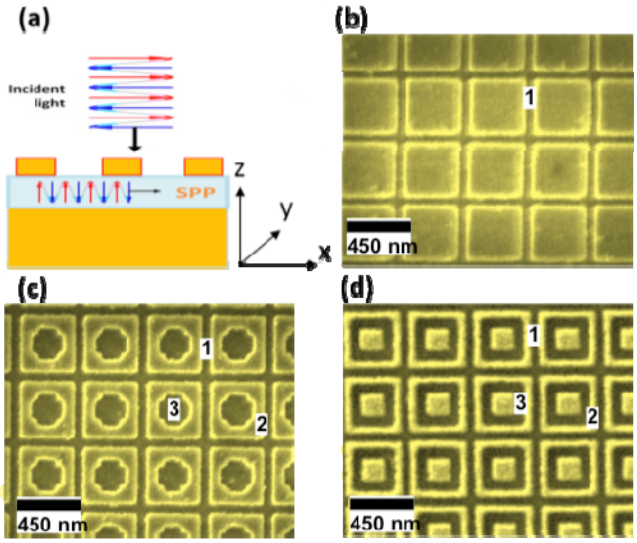


Fig. 1. (a) Schematic of GIM structure. False-colored SEM images of (b) box, (c) cross, and (d) box-in-box (BIB) grating structures, respectively. The numbers 1,2, and 3 correspond to the outer opening, outer Au frame, and inner opening, respectively.

## 2. Design and fabrication of the GIM structures

In order to systematically explore the effects of altering the unit cell in metamaterial structures, the square, cross, and BIB designs were implemented into a GIM structure, as shown in Fig. 1(a)-1(d). The purpose of this was three-fold: 1) to excite the GSPs via diffractive coupling, 2) to use the dielectric spacer layer to facilitate coupling between different geometric GSP modes when altering the unit cell, and 3) to provide a basic framework in which to explore unit cell modifications via nested geometries. SPPs can be directly excited by a metallic grating, which augments the wavevector, $k_x$, of the incident light with the wavevector of the SPP, $k_{sp}$, as shown, in [Eq. (1)]:

$$k_x = \frac{2\pi}{P}\eta_D \sin(\theta) \pm i\frac{2\pi}{P} \pm j\frac{2\pi}{P} = k_{sp}\frac{\omega}{c}\sqrt{\sum_m \frac{1}{\varepsilon_m(\lambda)}} \quad (1)$$

[Eq. (1)] uses the grating equation for a 2D square grating, where $i$ and $j$ are non-zero integers denoting the order of the grating modes in the $x$ and $y$ directions, respectively. As shown in the schematic in Fig. 1(a), when incident light is diffracted by the grating, the wavevector is oriented so that it matches the wavevector of the GSP, which exists between the two metal layers and is stimulated within the dielectric. Note that the right hand side of the equation has been expanded from the original SPP wavevector equation, since the dielectric constant term underneath the square root is just the sum/difference of the metal and dielectric constants. Here *m* refers to each individual material in the structure. In the case of the GIM, using *m* = 1,2,3 refers to the metal, dielectric, and the metamaterial grating, respectively, where the unit cell of the grating can be treated as an effective medium incorporating the index of air and metal with the corresponding fill fractions. In the case where the unit cell of the grating is a 2D geometric structure composed of a metal and the ambient, the dielectric function for the grating, $\varepsilon_g$, becomes $\varepsilon_g(x,y) + \varepsilon_{ambient}(x,y)$ and in the case of an effective medium treatment, $\varepsilon_g$ becomes $a\varepsilon_g + (1\text{-}a)\varepsilon_{ambient}$, where a is the filling factor of the metal of the unit cell.

Optics EXPRESS

Note that while [Eq. (1)] is expected to predict the modes for a simple two-dimensional square grating, it only factors in periodicity and not any symmetry of the unit cell, which significantly modifies the modes. Additionally, the back metal plane of the GIM structure facilitates the propagation of SPPs and enables the image charge of the localized SPPs from the grating structure, both of which are supported within the dielectric spacer layer. Therefore, when it comes to predicting modes of arbitrary nested geometries within a GIM, a more robust analytical model would be required.

For improved confinement of the GSP in the dielectric spacer, the evanescent decay of the SPP perpendicular to the metal surface, $z_i$, must be considered, and can be expressed by [Eq. (2)]:

$$z_i = \frac{\lambda}{2\pi}\sqrt{\frac{\left|\varepsilon_1^{'}\right| + \varepsilon_2}{\varepsilon_i^2}} \tag{2}$$

where $i$ = 1 or 2, representing the decay in the metal and dielectric, respectively. In the case of the dielectric, the higher the permittivity, the smaller the decay length and thus the higher the confinement. Using [Eq. (2)] and the permittivity for both air and sapphire ($Al_2O_3$), it was calculated that in the visible range, the confinement is approximately five times stronger in $Al_2O_3$ than in air. Therefore, 15 nm $Al_2O_3$ was used for the dielectric spacer.

Since the purpose of the grating was to study the polariton mode hybridization and its influence on the spectral dispersion of the metamaterial optical response, a simple 2D box grating was used as the primary base structure, allowing for simple modifications through inclusion of various structures within the unit cell. These modifications took the form of either perturbing the original grating by breaking the symmetry by adding a new structure that was dissimilar to the original square frame opening, or by replicating the original gap modes into the unit cell by adding a smaller square frame opening surrounding the original box. Importantly, the periodicity and original 2D grating widths were kept fixed in order to separate the effects of the grating from those of the modified unit cell, specifically the changes in modal character of the observed polaritonic resonances.

The GIM substrate was fabricated by first sonicating a Si substrate in acetone and isopropyl alcohol (IPA). The substrate was then coated with 100 nm Au using a Temescal FC-1800 electron beam evaporator, followed by 15 nm layer of $Al_2O_3$ using thermal atomic layer deposition (ALD), with a Beneq TSF200. A 300 nm layer of ZEP 520 A was spun over a clean Si wafer and prebaked at 180°C for 5 minutes. Box, cross, and BIB patterns were written using a Raith Voyager electron beam lithography system, with a dosage of 140 μC/cm$^2$. The pitch and box width of all three patterns were approximately 480 nm and 430 nm, respectively. The dimensions of the inclusions for the cross were two rectangles of 130 nm x 250 nm each, intersecting in the centers at right angles, as shown in Fig. 1(c). For the BIB, an inner gap of 80 nm on all sides was added, resulting in a square with a square frame, as shown in Fig. 1(d). The patterns were then developed using ZED N50 for 60s, followed by 60s of IPA rinsing. A bilayer of 3 nm Ti and 50 nm Au was deposited using electron beam evaporation at 1 Å/s and 2Å/s, respectively. Liftoff was performed using PG Remover overnight. SEM measurements, shown in Fig. 1(b)-1(d) were taken using a LEO scanning electron microscope (SEM) at 5kV.

## 3. Spectral and near-field analysis of similar vs dissimilar geometries in unit cell modifications

Reflectance measurements for the box, cross, and BIB structures were collected using a CRAIC microspectrophotometer, with a spectral range from approximately 856 THz (350 nm) to 176 THz (1700 nm) with all measurements referenced to the reflectance of an aluminum (Al) mirror. An aperture size of 20 um was used to limit the reflected light to only

Optics EXPRESS

that coming from the arrays of structures, with this aperture slightly smaller than the total array size to eliminate the potential for effects induced due to scattering off of the array edges. All spectra were normalized to the substrate in regions away from the arrays. These experimental reflectance measurements are provided in Fig. 2 as black traces for the (a) box, (b) cross, and (c) BIB structures. The GSP modes are labeled 1, 2, and 3, from left to right to assist in identifying and correlating the resonances between the various structures. The relative similarity between the box and cross spectra, which is absent in the comparison between the box and BIB spectra, is easily observed. The box structure shows three dominant peaks at approximately 250 THz (1200 nm), 375 THz (800 nm), and 440 THz (680 nm). Similarly, the cross structure shows the same highest wavelength peak, but with a slight blue-shift of approximately 10 THz. The higher frequency peaks, 2 and 3, are shifted approximately by 10 and 20 THz to the blue and red, respectively, appearing near 390 THz (768 nm) and 420 THz (714 nm). In addition, a significant decrease in amplitude is observed, most prominently for the 420 THz resonance. The spectral shifts, which only occur at the higher frequency regime, indicate that the GSPs of the box are perturbed resulting in some minor modifications due to the cross inclusion. The reflectance spectra for the BIB structure on the other hand, shows three dominant peaks at approximately 230 THz (1300 nm), 300 THz (1000 nm), and 375 THz (800 nm), with the lowest energy mode exhibiting a splitting indicating it is actually the result of two superimposed resonances. This splitting, along with the significantly modified spectral spread of the resonances with respect to those observed for the box and cross samples and the broadened linewidths imply that the modes observed in the BIB have been modified in a manner differently than the modes in the cross structure.

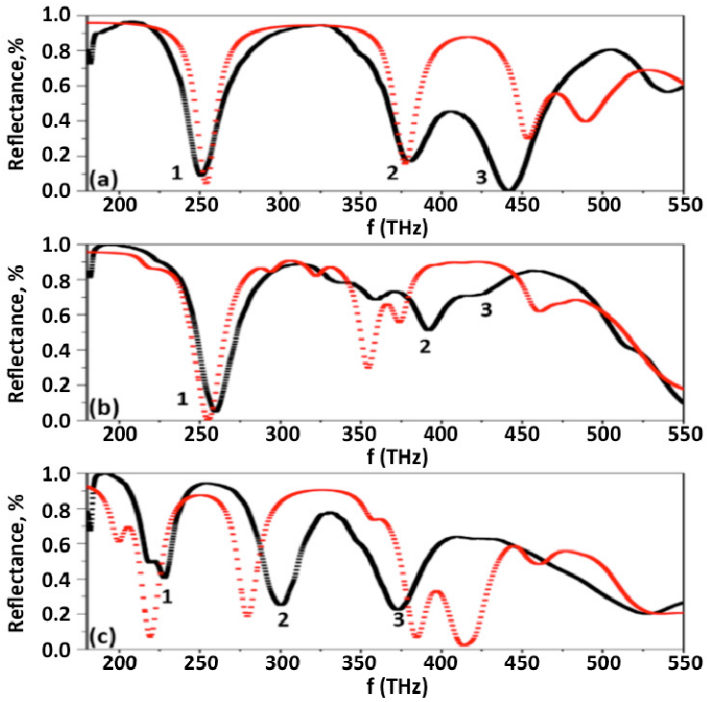


Fig. 2. Experimental (black) and simulated (red) reflectance spectra of (a) box, (b) cross, and (c) BIB, respectively. Modes are labeled from left to right.

To further understand the differences in the reflectance measurements, the spectra for each structure were calculated using Computer Simulation Technology (CST) Studio, with the RF and Microwave studio suite. S-parameters were calculated using the frequency domain, with open boundary conditions in the *z*-axis, and unit cell boundary conditions for the unit cell in

Optics EXPRESS

the $x$ and $y$ directions. The dimensions for the model were based on those taken from the experimental structures provided above in the text. The red spectra in Figs. 2(a)-2(c) correspond to those calculated for the box, cross, and BIB structures, respectively. The simulated and experimental spectra for the box grating show good qualitative agreement, except for the additional high-frequency fourth mode that is not observed in the experimental. In the cases of the cross and BIB structures, calculated and experimental spectra again show reasonable qualitative agreement, with a best match for the longest wavelength mode, as with the box structure, but for the higher energy modes, the simulated spectra are red-shifted by approximately 50 THz. It is possible that due to additional broadening in the experimental that the third and fourth peaks in the simulation for the BIB structure are actually observed as a single broad resonance mode. Note that although the modes in the BIB are not comparable to those of the box and cross, these modes are numbered in the same fashion. Due to the agreement in trends between calculated and experimental spectra for all three structures, the associated calculated electromagnetic field profiles from the spectra can be examined, which allow us to further understand the modifications caused by the cross and inner box inclusions.

The electric $E_z$ field profiles for the TM modes of the box, cross, and BIB structures are provided in Figs. 3(a)-3(c), respectively. The $E_z$ field profiles are presented for the cross-section located at the center of the sapphire layer, in a plane cut along the $x-y$ direction, using the same calculations presented in Fig. 2, with the orientation provided in Fig. 1(a). Overlaid with these fields is the calculated power flow (Poynting vector) for each respective mode. All modes are numbered 1, 2, and 3 to correspond with the numbered modes labeled in in the reflectance spectra in Fig. 2. Here we have ignored the highest frequency mode as these resonances were not observed experimentally. Agreeing with the reflectance spectra, there is a clear distinction between the resonant modes of each of these structures. In the cases of the box and cross structures, we find modes that exhibit decreasing polariton wavelength, indicating that the predominant impact on the field distributions for both box and cross structures is derived from the original box grating. In particular, the reduced wavelength implies that each successive mode is also a higher order of fundamental mode. However, beyond the similarities between the box and cross, there are multiple differences. While mode 1 for the cross structure shows a field distribution similar to that of the box, the fields are distorted and localized around the cross opening. For the higher order modes, the field distributions around the cross inclusion become increasingly localized, while maintaining the similar resonance frequency within the box structure. This correlates with the increasing spectral shifts in reflectance spectra between the cross and box for the higher order modes, as these near-field modifications due to the cross inclusion are predominantly observed at higher frequencies. This suggests that the new opening serves to modify the SPP fields and that there is some contribution from the cross GSPs at higher frequencies. The lower frequencies are not able to couple through the inclusion and instead the cross structure acts only as a minor perturbation to the original GSP from the grating. Significantly, the increasing effect of the cross opening at short wavelength modes implies an independence between the square and cross structures; at lower frequencies, we see spatial field contributions from the box, at higher frequencies, we see spatial contributions from the cross. This suggests that the new opening serves to modify the SPP fields and that the contribution from the cross GSPs is amplified at higher frequencies. For example, in the reflectance spectra, the line shape of the lowest resonant frequency mode was not significantly altered when going from the box to the cross structure. This means that dual-band or even multi-frequency metamaterials spanning large differences in frequency can be designed with independent operating frequencies by using contrasting geometries.

In contrast to the cross, the BIB structure exhibits fields that are simultaneously observed within both the inner box and outer frame partitions. Here, the lowest frequency resonance

Optics EXPRESS

exhibits a clear anti-phase relationship between the inner and outer parts, while for the higher frequency modes the fields become in-phase along the propagation direction (top to bottom as displayed). This suggests the opening that separates the inner box from the outer frame has a fundamentally different effect on the original grating than the center opening of the cross. In the case of the BIB, the GSPs do not continue around the inclusion, but instead form two distinct near-field patterns confined and redistributed over both distinct spatial regions of the modified unit cell. These two patterns are collective and exist at all resonance frequencies. The continued spatial contributions across the entire unit cell of the BIB across all three frequencies seems to imply a strong hybridization of the SPPs within the inner and outer box regions. This is further substantiated by the power-flow vectors. Note that in the case of the box and cross, the power-flow maintains a generally unified direction along the unit cell in the $x-y$ plane, whereas for the BIB, in all three modes, the directions of the power-flow in the inner and outer boxes are opposite to one another. In mode 1, the electric fields show the highest intensity underneath the inner box, whereas in modes 2 and 3 the intensity is highest in the region of the outer frame. Of interest is the drastic difference between the BIB and the box and cross structures, even for the lowest frequency mode 1. Whereas in the case of the cross structure, the longest SPP wavelength of the box was too large to couple with the cross inclusion, in all cases the BIB structure supports field profiles significantly altered by the presence of the inner box inclusion. This is a result of similar geometries, where matching frequencies and $k$ vectors allow for hybridization of the modes from the two complementary geometries. This is not the case in the cross structure, and therefore results in multiple distinct and independent resonances.

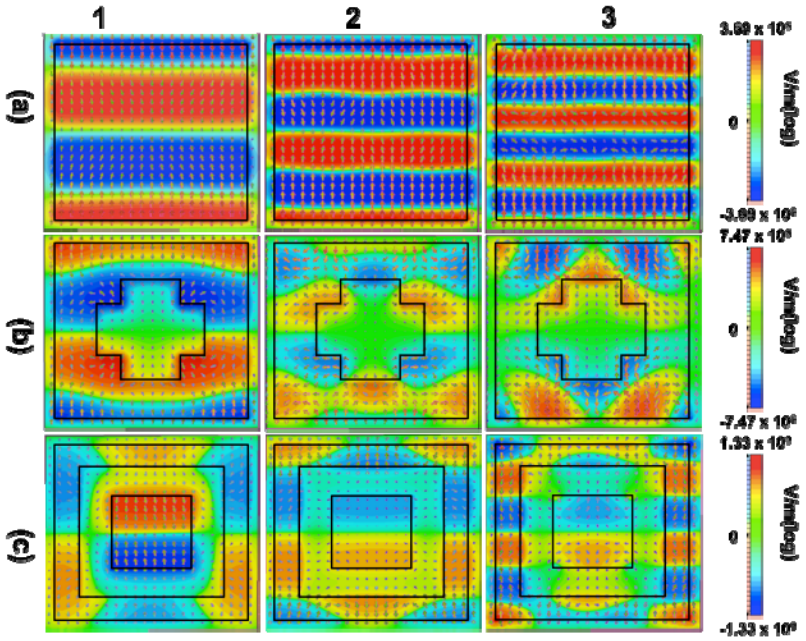


Fig. 3. Simulated $E_z$ field profiles in the center plane of the sapphire spacer and respective power flow of the (a) box, (b) cross, and (c) BIB structures. Modes are labeled 1-3 as in Fig. 2 for the simulated spectra. Outlines of the grating elements for the three structures have been drawn in for clarity.

## 4. Role of unit cell according to band structure

To better explore the modification of the simple geometries, the box, cross, and BIB structures can each be viewed as photonic crystals with repeating lattices based on the unit

Optics EXPRESS

cell, shown in the subset of Fig. 4(a), which uses the same dimensions as discussed above. In addition to calculating the band structures for the box, cross, and BIB structures, the band structures for the isolated cross opening (dissimilar element) and the isolated inner box opening (similar element) were also calculated individually in order to better understand the coupling effects between the simple box grating and the two different modifications (inner cross and inner box). The band structures were then calculated with Lumerical FDTD solutions, using a Lumerical planar 3D script file, where randomly oriented and distributed dipoles are used to excite the modes. Figure 4(a) provides the dispersion for the crystal structure based on the geometry shown beneath it. The $y$-axis shows frequency and the $x$-axis shows the $k$-vector along the $X$ point, which corresponds to one side of the unit cell in the $x$-direction, starting from the center (origin) of the box geometry, as indicated in the inset of Fig. 4(a). One hundred data points were taken along this line. The color ranges from blue (low) to red (high) and represents the coupling strength of electric dipole to the modes [41].

The bands in Fig. 4(a) correspond to the box geometry discussed here and exhibits modes at frequencies that closely match those in the experimental reflectance spectra for the box structure in Fig. 2. For ease in comparing the cross and BIB constructions, Fig. 4(a) is replicated as the first figure in both rows of Fig. 4. As discussed above, these modes are numbered according to their respective peaks in the experimental reflectance spectra of Fig. 2(b). Since the slope is dω/dk, this is equivalent to the group velocity and can therefore indicate the extent to which a mode is traveling or localized. The bands in Fig. 4(a) suggest that the box structure has both traveling and localized modes present, and also indicates their points of intersection along the unit cell. Note that in a random structure, $\omega = ck$ and the dispersion is linear. To account for randomness one would have to integrate over the *k*-vector and any photonic state will have contributions from all frequencies, while the localized states would have contributions only within a narrow energy band. Since band 1 is nominally dispersionless, this mode shown in the reflectance would likely not be strongly affected by reduced periodicity, as has been shown in similar cases with plasma-enhanced atomic layer deposited Ag [15,42,43], making structures with similar modes ideal candidates for fabrication.

Calculated band structures for the unit cell of an isolated cross, which is the basic subcell of our ‘cross’ structure, is provided in Fig. 4(b), with the full ‘cross’ structure provided in Fig. 4(c), as indicated by the schematics beneath each band structure. The modes are labeled for the final cross structure, according to their corresponding frequencies from the experimental reflectance spectra in Fig. 2(b). When examining the modes in Fig. 4(a)-4(c), it becomes clear that the final cross structure can be approximated as a simple summation of the modes from the cross inclusion and the original box. In fact, the band structure in Fig. 4(c) qualitatively appears as a superposition of these two previous band structures. As expected for two dissimilar geometries, the bands present in the grating in Fig. 4(a) and the bands in the cross exclusion in Fig. 4(b) have little spectral interactions, and thus their combination is just the sum of the two, rather than the formation of new hybrid modes. This is supported by the field profiles for the box and cross in Fig. 3(a) and 3(b), respectively, where the two different geometries show modes that largely operate independently. The isolated cross inclusion only shows one strong band, which is at approximately 500 THz (600 nm), which also appears in the full ‘cross’ band structure as well. This band was not seen in the reflectance as it was outside the CRAIC microspectrophotometer detection range, but demonstrates the uncoupled additive nature of the modes, making it ideal for multi-band design, with separate control of the spatial and spectral response. The bands for the isolated inner box structure (square opening), Fig. 4(d), are closer in number, intensity, and frequency to the bands of the original box structure in Fig. 4(a) than are the bands of the cross inclusion. This is expected as both geometries are similar in structure. Significantly, Fig. 4(e), which shows the dispersion for the full BIB structure, exhibits a significantly different band structure than either the original box

Optics EXPRESS

or inner box that it comprises. As with the original box and cross band structures, these bands are labeled with respect to the reflectance modes of matching frequencies. Unlike the cross structure, the SPPs observed in the BIB cannot be simply described as a summation of those from the inner and outer box structures. Band 3 in particular appears uniquely different from any of those present in either the outer frame of Fig. 4(a) or for the isolated inner box structure of Fig. 4(d). This suggests that at least some of the bands in the final BIB structure are a result of hybridization between the SPPs within the inner and outer components, resulting in new modes with different degrees of localization. This mode hybridization is clearly distinguishable from additive modes when looking at the different band structures, thereby demonstrating the potential for this methodology for qualifying polaritonic behaviors in periodic structures. The field hybridization observed in the band structures for the BIB structure is supported by the respective field profiles in Fig. 3(c), which show modes that are dependent on the entirety of the modified unit cell. However, it is important to note that only the band structure provides an unambiguous analysis of mode hybridization when comparing a structure and its constituent components, as it provides both the spatial and spectral elements simultaneously. In the case of analyzing a structure with two nested geometries, one can potentially determine hybridization using just three calculations.

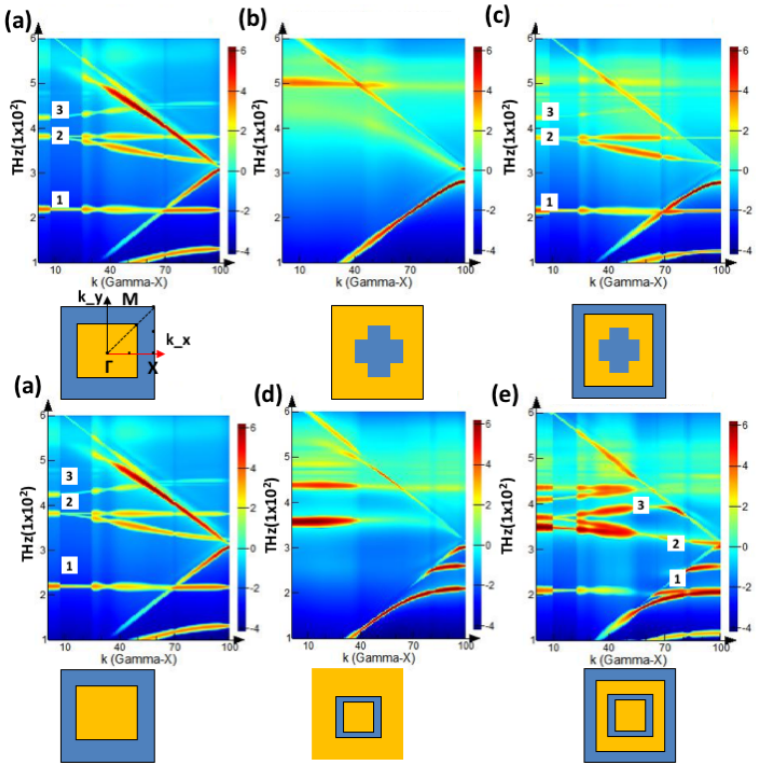


Fig. 4. Calculated band structures for (a) box structure, (b), (c) cross opening and final cross structure, and (d), (e) box opening and final BIB structure. The respective geometries used for each band structure are showed beneath, including a schematic of the unit cell for the original box structure. The edge along which the band structures were calculated is highlighted in red. The band structures for the constituent geometries, (b) and (d), demonstrate the additive and coupling natures of the cross and BIB structures, respectively. (a) has been added in both rows for direct comparison.

In summary, by fabricating different unit cell geometries in GIM structures, we have been able to examine GSP interactions within nested structures of both complementary and dissimilar geometries. It was shown that the dissimilar geometries shown here, when nested,

Optics EXPRESS

resulted in only slight modifications to their respective near-field patterns, which enables the potential for adding new modes to a structure that are independent of one another. In contrast, the nested, similar geometries studied resulted in an entirely new set of resonances that were the result of both additive and hybridization effects between the various near-fields. The new modes were not just different spectrally, but also in terms of the spatial distributions of the fields in the unit cell, the extent of the localized and traveling characteristics, and modes that potentially exhibit both. This is an important tuning knob for designing metamaterials for multi resonant structures and/or designing devices with a more complex system of near-field patterns. Specifically, the ability to collocate or separate the local near-fields at different frequencies can have significant implications for enhancing spatially segregated emitters, or for enhancing emitters at two distinct frequencies, e.g. as in upconversion processes. The implementation of nested geometries into two-dimensional gratings could also be used to improve path length and or directionality [44] for increased quantum efficiency in grating-enhanced photodetectors [45] or polaritonic narrow-band thermal emitters [46–48]. Significantly, the band structure of the plasmonic unit cell provides an alternative tool to simulations of reflectance spectra and correlated field profiles, offering a compact, quantitative analysis of both spectral and spatial dispersion of the GSP response. This includes simplified analysis of the modal coupling within the nested geometries discussed here, specifically the degree of localization or propagation via analysis of the group velocity. Further, the spectral component potentially simplifies the modeling process as field character information is provided simultaneously, rather than sequentially, allowing for an easy platform to calculate the mode nature as a function of geometric properties.

## Funding

Office of Naval Research (ONR) (N0001412WX20514); National Academies of Sciences, Engineering, and Medicine

## Acknowledgments

The author N. Sharac acknowledges support from the National Research Council (NRC) NRL Postdoctoral Fellowship Programs.

## References

1. S. A. Maier, *Plasmonics: Fundamentals and Applications* (Springer US, 2007).
2. M. L. Brongersma and V. M. Shalaev, "The case for plasmonics," Science **328**(5977), 440–441 (2010).
3. F. Wu, W. Wang, J. Hua, Z. Xu, and F. Li, "Control on Surface Plasmon Polaritons Propagation Properties by Continuously Moving a Nanoparticle along a Silver Nanowire Waveguide," Sci. Rep. **6**(1), 37512 (2016).
4. A. Rose, T. B. Hoang, F. McGuire, J. J. Mock, C. Ciracì, D. R. Smith, and M. H. Mikkelsen, "Control of Radiative Processes Using Tunable Plasmonic Nanopatch Antennas," Nano Lett. **14**(8), 4797–4802 (2014).
5. J. B. Lassiter, F. McGuire, J. J. Mock, C. Ciracì, R. T. Hill, B. J. Wiley, A. Chilkoti, and D. R. Smith, "Plasmonic Waveguide Modes of Film-Coupled Metallic Nanocubes," Nano Lett. **13**(12), 5866–5872 (2013).
6. X. Chen, C. Ciracì, D. R. Smith, and S.-H. Oh, "Nanogap-Enhanced Infrared Spectroscopy with Template-Stripped Wafer-Scale Arrays of Buried Plasmonic Cavities," Nano Lett. **15**(1), 107–113 (2015).
7. R. T. Hill, J. J. Mock, Y. Urzhumov, D. S. Sebba, S. J. Oldenburg, S.-Y. Chen, A. A. Lazarides, A. Chilkoti, and D. R. Smith, "Leveraging Nanoscale Plasmonic Modes to Achieve Reproducible Enhancement of Light," Nano Lett. **10**(10), 4150–4154 (2010).
8. X. Chen, H.-R. Park, M. Pelton, X. Piao, N. C. Lindquist, H. Im, Y. J. Kim, J. S. Ahn, K. J. Ahn, N. Park, D.-S. Kim, and S.-H. Oh, "Atomic layer lithography of wafer-scale nanogap arrays for extreme confinement of electromagnetic waves," Nat. Commun. **4**(1), 2361 (2013).
9. H. Im, K. C. Bantz, N. C. Lindquist, C. L. Haynes, and S.-H. Oh, "Vertically Oriented Sub-10-nm Plasmonic Nanogap Arrays," Nano Lett. **10**(6), 2231–2236 (2010).
10. D. Yoo, N.-C. Nguyen, L. Martin-Moreno, D. A. Mohr, S. Carretero-Palacios, J. Shaver, J. Peraire, T. W. Ebbesen, and S.-H. Oh, "High-Throughput Fabrication of Resonant Metamaterials with Ultrasmall Coaxial Apertures via Atomic Layer Lithography," Nano Lett. **16**(3), 2040–2046 (2016).
11. F. Ding, Y. Yang, R. A. Deshpande, and S. I. Bozhevolnyi, "A review of gap-surface plasmon metasurfaces: fundamentals and applications," Nanophotonics **7**, 1129 (2018).
12. T. Søndergaard, J. Jung, S. I. Bozhevolnyi, and G. D. Valle, "Theoretical analysis of gold nano-strip gap plasmon resonators," New J. Phys. **10**(10), 105008 (2008).

Optics EXPRESS


13. Y. Lu, W. Dong, Z. Chen, A. Pors, Z. Wang, and S. I. Bozhevolnyi, "Gap-plasmon based broadband absorbers for enhanced hot-electron and photocurrent generation," Sci. Rep. **6**(1), 30650 (2016).
14. Y. Zhai, G. Chen, J. Xu, Z. Qi, X. Li, and Q. Wang, "Multiple-band perfect absorbers based on the combination of Fabry-Perot resonance and the gap plasmon resonance," Opt. Commun. **399**, 28–33 (2017).
15. J. D. Caldwell, O. J. Glembocki, F. J. Bezares, M. I. Kariniemi, J. T. Niinistö, T. T. Hatanpää, R. W. Rendell, M. Ukaegbu, M. K. Ritala, S. M. Prokes, C. M. Hosten, M. A. Leskelä, and R. Kasica, "Large-area plasmonic hot-spot arrays: sub-2 nm interparticle separations with plasma-enhanced atomic layer deposition of Ag on periodic arrays of Si nanopillars," Opt. Express **19**(27), 26056–26064 (2011).
16. J. D. Caldwell, O. Glembocki, F. J. Bezares, N. D. Bassim, R. W. Rendell, M. Feygelson, M. Ukaegbu, R. Kasica, L. Shirey, and C. Hosten, "Plasmonic Nanopillar Arrays for Large-Area, High-Enhancement Surface-Enhanced Raman Scattering Sensors," ACS Nano **5**(5), 4046–4055 (2011).
17. A. B. Zrimsek, A.-I. Henry, and R. P. Van Duyne, "Single Molecule Surface-Enhanced Raman Spectroscopy without Nanogaps," J. Phys. Chem. Lett. **4**(19), 3206–3210 (2013).
18. "Surface-enhanced Raman spectroscopy for in vivo biosensing | Nature Reviews Chemistry," https://www.nature.com/articles/s41570-017-0060.
19. C. Zong, M. Xu, L.-J. Xu, T. Wei, X. Ma, X.-S. Zheng, R. Hu, and B. Ren, "Surface-Enhanced Raman Spectroscopy for Bioanalysis: Reliability and Challenges," Chem. Rev. **118**(10), 4946–4980 (2018).
20. D. Yoo, D. A. Mohr, F. Vidal-Codina, A. John-Herpin, M. Jo, S. Kim, J. Matson, J. D. Caldwell, H. Jeon, N.-C. Nguyen, L. Martin-Moreno, J. Peraire, H. Altug, and S.-H. Oh, "High-Contrast Infrared Absorption Spectroscopy via Mass-Produced Coaxial Zero-Mode Resonators with Sub-10 nm Gaps," Nano Lett. **18**(3), 1930–1936 (2018).
21. J. M. Hoffmann, H. Janssen, D. N. Chigrin, and T. Taubner, "Enhanced infrared spectroscopy using small-gap antennas prepared with two-step evaporation nanosphere lithography," Opt. Express **22**(12), 14425–14432 (2014).
22. M. Autore, P. Li, I. Dolado, F. J. Alfaro-Mozaz, R. Esteban, A. Atxabal, F. Casanova, L. E. Hueso, P. Alonso-González, J. Aizpurua, A. Y. Nikitin, S. Vélez, and R. Hillenbrand, "Boron nitride nanoresonators for phonon-enhanced molecular vibrational spectroscopy at the strong coupling limit," Light Sci. Appl. **7**(4), 17172 (2018).
23. R. Adato and H. Altug, "*In-situ* ultra-sensitive infrared absorption spectroscopy of biomolecule interactions in real time with plasmonic nanoantennas," Nat. Commun. **4**(1), 2154 (2013).
24. X. Ni, Z. J. Wong, M. Mrejen, Y. Wang, and X. Zhang, "An ultrathin invisibility skin cloak for visible light," Science **349**(6254), 1310–1314 (2015).
25. L. Lin and Y. Zheng, "Optimizing plasmonic nanoantennas via coordinated multiple coupling," Sci. Rep. **5**, 14788 (2015).
26. X. Liu and W. J. Padilla, "Dynamic Manipulation of Infrared Radiation with MEMS Metamaterials," Advanced Optical Materials **1**(8), 559–562 (2013).
27. R. Nicolas, G. Lévêque, J. Marae-Djouda, G. Montay, Y. Madi, J. Plain, Z. Herro, M. Kazan, P.-M. Adam, and T. Maurer, "Plasmonic mode interferences and Fano resonances in Metal-Insulator-Metal nanostructured interface," Sci. Rep. **5**(1), 14419 (2015).
28. "Electrically Tunable Gap Surface Plasmon-based Metasurface for Visible Light | Scientific Reports," https://www.nature.com/articles/s41598-017-14583-7.
29. A. Pors, F. Ding, Y. Chen, I. P. Radko, and S. I. Bozhevolnyi, "Random-phase metasurfaces at optical wavelengths," Sci. Rep. **6**(1), 28448 (2016).
30. A. Pors and S. I. Bozhevolnyi, "Plasmonic metasurfaces for efficient phase control in reflection," Opt. Express **21**(22), 27438–27451 (2013).
31. L. Langguth, D. Punj, J. Wenger, and A. F. Koenderink, "Plasmonic Band Structure Controls Single-Molecule Fluorescence," ACS Nano **7**(10), 8840–8848 (2013).
32. M. Javaid and T. Iqbal, "Plasmonic Bandgap in 1D Metallic Nanostructured Devices," Plasmonics **11**(1), 167–173 (2016).
33. D. J. Park, C. Zhang, J. C. Ku, Y. Zhou, G. C. Schatz, and C. A. Mirkin, "Plasmonic photonic crystals realized through DNA-programmable assembly," Proc. Natl. Acad. Sci. U.S.A. **112**(4), 977–981 (2015).
34. W. Wang, D. Zhao, Y. Chen, H. Gong, X. Chen, S. Dai, Y. Yang, Q. Li, and M. Qiu, "Grating-assisted enhanced optical transmission through a seamless gold film," Opt. Express **22**(5), 5416–5421 (2014).
35. Y.-J. Chang, "Design and analysis of metal/multi-insulator/metal waveguide plasmonic Bragg grating," Opt. Express **18**(12), 13258–13270 (2010).
36. N. Liu, M. Mesch, T. Weiss, M. Hentschel, and H. Giessen, "Infrared Perfect Absorber and Its Application as Plasmonic Sensor," Nano Lett. **10**(7), 2342–2348 (2010).
37. J. Hao, J. Wang, X. Liu, W. J. Padilla, L. Zhou, and M. Qiu, "High performance optical absorber based on a plasmonic metamaterial," Appl. Phys. Lett. **96**(25), 251104 (2010).
38. P. Nordlander, C. Oubre, E. Prodan, K. Li, and M. I. Stockman, "Plasmon Hybridization in Nanoparticle Dimers," Nano Lett. **4**(5), 899–903 (2004).
39. Q. Li and Z. Zhang, "Bonding and Anti-bonding Modes of Plasmon Coupling Effects in $TiO_2$-Ag Core-shell Dimers," Sci. Rep. **6**(1), 19433 (2016).
40. W. Zhou, J. Y. Suh, Y. Hua, and T. W. Odom, "Hybridization of Localized and Guided Modes in 2D Metal–Insulator–Metal Nanocavity Arrays," J. Phys. Chem. C **117**(6), 2541–2546 (2013).

Optics EXPRESS


41. D. Lu, A. Das, and W. Park, "Direct modeling of near field thermal radiation in a metamaterial," Opt. Express **25**(11), 12999–13009 (2017).
42. S. M. Prokes and O. J. Glembocki, "Self Assembled Metamaterials Formed via Plasma Enhanced ALD of Ag Thin Films," ECS Trans. **64**(9), 279–289 (2014).
43. S. M. Prokes, O. J. Glembocki, E. Cleveland, J. D. Caldwell, E. Foos, J. Niinistö, and M. Ritala, "Spoof-like plasmonic behavior of plasma enhanced atomic layer deposition grown Ag thin films," Appl. Phys. Lett. **100**(5), 053106 (2012).
44. A. G. Curto, G. Volpe, T. H. Taminiau, M. P. Kreuzer, R. Quidant, and N. F. van Hulst, "Unidirectional Emission of a Quantum Dot Coupled to a Nanoantenna," Science **329**(5994), 930–933 (2010).
45. E. M. Jackson, J. A. Nolde, M. Kim, C. S. Kim, E. R. Cleveland, C. A. Affouda, C. L. Canedy, I. Vurgaftman, J. R. Meyer, E. H. Aifer, and J. Lorentzen, "Two-dimensional plasmonic grating for increased quantum efficiency in midwave infrared nBn detectors with thin absorbers," Opt. Express **26**(11), 13850–13864 (2018).
46. T. Wang, P. Li, D. N. Chigrin, A. J. Giles, F. J. Bezares, O. J. Glembocki, J. D. Caldwell, and T. Taubner, "Phonon-Polaritonic Bowtie Nanoantennas: Controlling Infrared Thermal Radiation at the Nanoscale," ACS Photonics **4**(7), 1753–1760 (2017).
47. J.-J. Greffet, R. Carminati, K. Joulain, J.-P. Mulet, S. Mainguy, and Y. Chen, "Coherent emission of light by thermal sources," Nature **416**(6876), 61–64 (2002).
48. S. Molesky, C. J. Dewalt, and Z. Jacob, "High temperature epsilon-near-zero and epsilon-near-pole metamaterial emitters for thermophotovoltaics," Opt. Express **21**(S1), A96–A110 (2013).


132.250.22.8 {ts '2020-07-09 08:34:10'}